

Advancing Autonomous Navigation: Near-Moon GNSS-based Orbit Determination

*Original*

Advancing Autonomous Navigation: Near-Moon GNSS-based Orbit Determination / Vouch, Oliviero; Nardin, Andrea; Minetto, Alex; Zocca, Simone; Dosis, Fabio; Konitzer, Lauren; Parker, Joel J. K.; Ashman, Benjamin; Bernardi, Fabio; Tedesco, Simone; Fantinato, Samuele; Facchinetti, Claudia. - ELETTRONICO. - (2024), pp. 3277-3291. (Intervento presentato al convegno 37th International Technical Meeting of the Satellite Division of The Institute of Navigation (ION GNSS+ 2024) tenutosi a Baltimore, Maryland (USA) nel September 16-20, 2024) [10.33012/2024.19814].

*Availability:*

This version is available at: 11583/2991133 since: 2024-10-30T14:19:40Z

*Publisher:*

The Institute of Navigation (ION)

*Published*

DOI:10.33012/2024.19814

*Terms of use:*

This article is made available under terms and conditions as specified in the corresponding bibliographic description in the repository

*Publisher copyright*

GENERICO -- per es. EPJ (European Physical Journal) : quando richiesto un rinvio generico specifico per

(Article begins on next page)

# Advancing Autonomous Navigation: Near-Moon GNSS-based Orbit Determination

Oliviero Vouch<sup>1</sup>, Andrea Nardin<sup>1</sup>, Alex Minetto<sup>1</sup>, Simone Zocca<sup>1</sup>, Fabio Dovis<sup>1</sup>, Lauren Konitzer<sup>2</sup>, Joel J.K. Parker<sup>2</sup>, Benjamin Ashman<sup>2</sup>, Fabio Bernardi<sup>3</sup>, Simone Tedesco<sup>3</sup>, Samuele Fantinato<sup>3</sup>, and Claudia Facchinetti<sup>4</sup>

<sup>1</sup>*Department of Electronics and Telecommunications (DET), Politecnico di Torino, Torino, Italy*

<sup>2</sup>*NASA Goddard Space Flight Center, Greenbelt, Maryland, USA*

<sup>3</sup>*Qascom SRL, Bassano del Grappa, Vicenza, Italy*

<sup>4</sup>*Italian Space Agency (ASI–Agenzia Spaziale Italiana), Roma, Italy*

## BIOGRAPHY

**Oliviero Vouch** is a Ph.D. student working with the Navigation Signal Analysis and Simulation (NavSAS) group. His research interests cover advanced Bayesian estimation applied to multi-sensor integrated navigation units based on Global Navigation Satellite System (GNSS).

**Andrea Nardin** is Assistant Professor at the Department of Electronics and Telecommunications of Politecnico di Torino where he has been working with the NavSAS group since 2018. His research interests include signal processing architectures and signal design applied to GNSSs and LEO PNT.

**Alex Minetto** joined the Department of Electronics and Telecommunications of Politecnico di Torino, in 2021 as a Researcher and Assistant Professor. His current research interests cover navigation signal design and processing, advanced Bayesian estimation applied to positioning, navigation, and timing technologies.

**Simone Zocca** is a Ph.D. student within the NavSAS group at the Department of Electronics and Telecommunications of Politecnico di Torino. His research is focused on innovative solutions for signal processing techniques and Bayesian estimation applied to Global Navigation Satellite System (GNSS).

**Fabio Dovis** is Full Professor at the Department of Electronics and Telecommunications, Politecnico di Torino. He coordinates the NavSAS Group and is Co-PI of the LuGRE project. His research interests include design of GPS and Galileo receivers and advanced signal processing for interference and multipath detection and mitigation, and also ionospheric monitoring.

**Lauren Konitzer** is a Navigation and Mission Design Engineer at NASA Goddard Space Flight Center. She is the Deputy Principal Investigator for the Lunar GNSS Receiver Experiment (LuGRE).

**Joel J.K. Parker** is a Senior Navigation Engineer in the Navigation and Mission Design Branch at NASA GSFC. He is the LuGRE Principal Investigator (PI).

**Benjamin Ashman** is a Navigation Engineer in the Navigation and Mission Design Branch at NASA GSFC, and was the 2021–2022 ION/AAAS Congressional Science and Engineering Fellow. He is a member of the LuGRE PI team.

**Fabio Bernardi** is a Radio Navigation Engineer in the Advanced Navigation Unit at Qascom. He is involved in the LuGRE payload.

**Simone Tedesco** is a Radio Navigation Engineer in the Advanced Navigation Unit at Qascom. He is involved in the LuGRE payload.

**Samuele Fantinato** is Head of the Advanced Navigation Unit at Qascom. He is Program/Project Manager (PM) of the LuGRE payload.

**Claudia Facchinetti** leads the Engineering, Cost Analysis & CEF Office within the Engineering and Future Space Systems Unit at ASI. She is the Agenzia Spaziale Italiana (ASI–Italian Space Agency) Project Manager of the LuGRE Payload.

## ABSTRACT

Global Navigation Satellite Systems (GNSSs) have settled as a crucial asset for Positioning, Navigation and Timing (PNT) within the Space Service Volume (SSV), and this technology is increasingly recognized a major player to serve the realm of lunar exploration missions. Current space operations are heavily relying on ground infrastructures, with escalating operational costs and limited resources. Therefore, it is urgent to enhance autonomy of space users, particularly in the task of real-time Orbit Determination (OD). This study aims to demonstrate the performance of GNSS-based onboard OD in the lunar regime. In a sequential Bayesian architecture, where GNSS observations are filtered with an orbital propagator, the sigma-point Unscented

44 Kalman Filter (UKF) model is compared against the renowned Extended Kalman Filter (EKF)-based Orbital Filter (OF). The  
45 upcoming LuGRE mission serves as a case study, showcasing near-Moon PNT from a simulated portion of lunar ignition  
46 orbit at approximately 61 Earth Radii (RE). Both navigation algorithms are assessed with actual receiver observables, retrieved  
47 from a high-fidelity Hardware-in-the-Loop (HIL) simulation. Results highlight that the UKF effectively smooths out harmful  
48 Dilution of Precision (DOP) leaps induced by losses of lock of some GNSS signals, while maintaining position estimation errors  
49 within 2 km for 98.97% of the time. Moreover, remarkable accuracy gains over the EKF are observed, with a  $3\sigma$  percentile  
50 improvement of 79.97% for position estimates and 63.62% for velocity estimates.

## I. INTRODUCTION

51 In contemporary space operations, the navigation, guidance, and maneuvering of space vehicles largely depend on ground  
52 segment assets. Radio Frequency (RF) tracking via Deep Space Networks (DSNs) facilities and Direct-to-Earth (DTE) links  
53 enables advanced Orbit Determination (OD) techniques through sophisticated off-board processing algorithms (Iess et al., 2014).  
54 However, relying on ground-segment assets introduces several drawbacks. Operational costs are elevated, and the management  
55 of numerous missions is constrained by limited ground segment resources (Turan et al., 2022). To meet the objectives set by the  
56 space exploration roadmap, there is a pressing need to enhance autonomous navigation capabilities.

57 In the Space Service Volume (SSV), Global Navigation Satellite Systems (GNSSs) are a crucial asset for autonomous spacecraft  
58 (S/C) navigation and timing, and their usage has been regulated up to Geosynchronous Orbit (GEO) altitudes (Parker et al.,  
59 2018). While processing of Earth's GNSS signal in space has been proven feasible at higher altitudes, several technological  
60 challenges arise. The Earth's obstruction of satellite signals determines drops of availability. Moreover, the increased free-space  
61 path loss attenuation together with frequent tracking of side lobes results in weak signal reception and noisy observations.  
62 Additionally, the unfavourable geometric diversity of ranging sources can exacerbate navigation uncertainty.

63 Targeting the lunar regime, scientific literature has proposed sequential filtering architectures to address the challenges of  
64 ground-independent and precise OD using onboard GNSS radiometric observations. Extended Kalman Filter (EKF)-based  
65 Orbital Filter (OF) models, as pioneered by (Capuano, 2016), have demonstrated significant navigation performance in Earth-  
66 Moon transfer orbit (MTO) up to Moon altitudes. In line with the reduced dynamic approach, (Capuano et al., 2017) augmented  
67 the state space model with pseudo-stochastic parameters to mitigate the effects of unmodeled or mismodeled S/C dynamics.  
68 Additionally, an ensemble Kalman filter (EnKF) model targeting orbital navigation in MTO has shown promising performance  
69 in simulations at lunar altitudes (Murata, 2023). Recently, unconventional EKF architectures that constrain a kinematic OD  
70 solution with a planned orbital trajectory have also been proposed (Vouch et al., 2024).

71 As part of National Aeronautics and Space Administration (NASA)'s Commercial Lunar Payload Services (CLPS) program  
72 (Task Order 19D), the Lunar GNSS Receiver Experiment (LuGRE) (Parker et al., 2022) serves as case study to investigate the  
73 potential of more advanced Bayesian formulations for autonomous GNSS-based orbital navigation of a S/C in lunar proximity.  
74 The LuGRE technology development payload will deploy the Navigation Early Investigation on Lunar surface (NEIL) module—a  
75 GNSS Software Defined Radio (SDR) receiver specifically customized for operations in deep-space (Tedesco et al., 2023)—  
76 onboard the US Firefly Blue Ghost Mission 1 (BGM1) lander. The mission aims to be the first flight demonstration of  
77 multi-GNSS PNT in cis-lunar space and on the Moon surface; one of the key scientific objectives of LuGRE is to assess  
78 the performance of filtering-based PNT solutions obtained both by the real-time receiver operation and through ground-based  
79 post-processing of sampled multi-system, multi-band observables (Minetto et al., 2022; Nardin et al., 2022, 2023).

80 This work explores the potential of a more complex Unscented Kalman Filter (UKF) model which integrates multi-channel  
81 GNSS observables tightly with the prediction of space dynamics from an orbital propagator. Benchmarking the UKF formulation  
82 against an EKF-based model, a Low Lunar Orbit (LLO) segment 61 RE away from Earth is considered to comprehensively  
83 assess the attainable orbital navigation performance. In particular, both Bayesian estimators are tested for the post-processing of  
84 observables constructed by the LuGRE receiver in a Hardware-in-the-Loop (HIL) simulation with RF GNSS signals. Leveraging  
85 a faithful model for the RF link simulation, the operational environment seen by a receiver in lunar proximity is also discussed  
86 in terms of navigation metrics. Even with an error-prone initialization, the UKF-based architecture can effectively tackle harsh  
87 multilateration geometry and reduced availability exhibiting position estimation errors within 2 km for the 98.97% of the  
88 analyzed orbit.

## II. BACKGROUND

89 From the navigation perspective, OD is the problem of determining the S/C motion relative to the center of mass of the Earth,  
90 and express it in a specified coordinate system. Orbital motion is described by the state of the dynamical system, which  
91 encompasses the instantaneous S/C position and velocity as minimal set of parameters useful to predict future motion states.  
92 In a Bayesian filtering framework, GNSS-based orbital navigation can be framed as a statistical estimation process which  
93 sequentially estimates the belief of the latent system state. Given an initial estimate  $x_0$  of the state drawn from a distribution

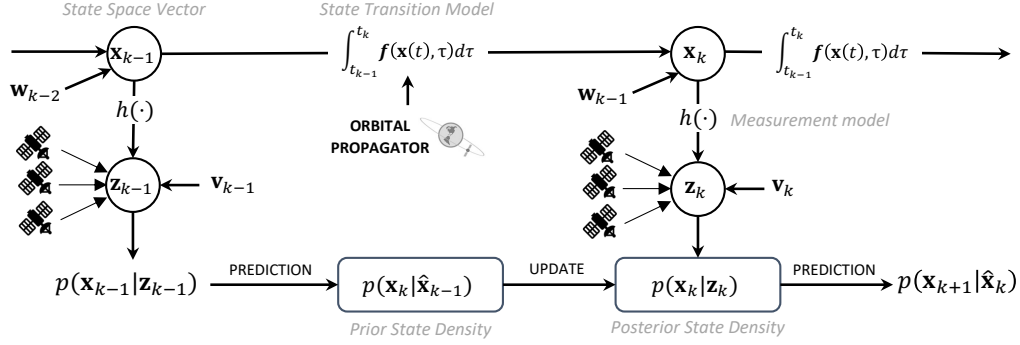


**Figure 1:** Bayesian filtering approach for orbital navigation with radiometric GNSS observations, integrating predictions from an orbital propagation model. Inspired by (Fang et al., 2018).

94  $p(\mathbf{x}_0)$  which reflects the initial knowledge about the system (i.e., the initial condition), the estimation process tackled by the  
 95 Bayesian filter follows two steps:

- 96 • **Prediction of the prior state density:** the moments of the prior  $p(\mathbf{x}_k|\hat{\mathbf{x}}_{k-1})$ <sup>1</sup> predict the system state evolution at time  
 97  $t_k$  by applying the transitional model  $\mathbf{f}(\cdot)$  to the latest state estimate  $\hat{\mathbf{x}}_{k-1}$ .
- 98 • **Estimation of the posterior state density:** the posterior  $p(\mathbf{x}_k|\mathbf{z}_k)$  is estimated leveraging sampled observations  $\mathbf{z}_k$  which  
 99 relate to the state through the measurement model  $\mathbf{h}(\cdot)$ .

100 A mathematical formulation of the S/C orbital dynamics (i.e., an *orbital propagator*) defines the transitional (or, motion) model  
 101 as a non-linear, stochastic differential equation:

$$\dot{\mathbf{x}}(t) = \mathbf{f}(\mathbf{x}(t), t) + \mathbf{w}(t) . \quad (1)$$

102 Inaccuracies in the physical model of the orbital forces would end up causing the orbital propagator to deviate from the actual  
 103 motion. These effects, together with deterministic yet unknown control inputs, are captured in the process noise term  $\mathbf{w}(t)$ .  
 104 As a matter of fact, (1) is a transitional model with continuous-time dynamics. Although the orbital motion is more accurately  
 105 described in continuous-time, the system is observed at discrete-time instants. When an estimate of the orbiting vehicle state is  
 106 available at  $t_{k-1}$ , (1) can be numerically integrated (cf. (Battin, 1999)) between sample intervals:

$$\mathbf{x}_k = \mathbf{x}_{k-1} + \int_{t_{k-1}}^{t_k} \mathbf{f}(\mathbf{x}(t), \tau) d\tau + \mathbf{w}_k . \quad (2)$$

107 Model (2) characterizes the system evolution in terms of an equivalent non-linear, discrete-time difference equation. The  
 108 random white-noise sequence  $\mathbf{w}_k$  is considered from the discretization of a piecewise constant process noise (Schutz et al.,  
 109 2004). Under the assumption that the system state evolves as a discrete-time Markov process, a graphical representation of the  
 110 sequential procedure is shown in Figure 1.

111 When sampled GNSS observations are retrieved onboard (i.e.,  $\mathbf{z}_k$ ), they are processed through the measurement model:

$$\mathbf{z}_k = \mathbf{h}_k(\mathbf{x}_k) + \mathbf{v}_k . \quad (3)$$

112 This model filters observations using predictions based on orbital propagation, treating non-systematic measurement errors as  
 113 additive disturbances with runtime-adaptable covariance. The resulting Bayesian formulation integrates GNSS observables  
 114 tightly with the prediction of space dynamics (Capuano, 2016). This approach is well-suited at lunar altitudes where GNSS  
 115 signal depletion occurs and blind spots are likely to intermittently appear. In fact, the integration of an orbital propagator enables  
 116 continuous navigation without the need for a minimum set of radiometrically visible satellites to compute a single-point solution.  
 117 Additionally, a limited number of measurements can still be beneficial in constraining the model-based orbital propagation,  
 118 provided these measurements are not outliers. This helps to prevent drift caused by the integration of process noise.

<sup>1</sup> $\mathbf{x}_k = \mathbf{x}(t = t_k)$ , and  $\hat{\mathbf{x}}_k$  is an estimate of the true yet unknown system state.

## 1. Space vehicle dynamics

In the framework of Newtonian's physics, the S/C motion dynamics in an inertial reference frame relative to the Earth's center of mass are governed by the two-body model:

$$\ddot{\mathbf{r}}(t) = -\frac{GM_e \mathbf{r}(t)}{r(t)^3} = -\frac{\mu_e \mathbf{r}(t)}{r(t)^3} \quad (4)$$

which defines the second-order differential equation of motion for the unperturbed Keplerian orbit. In particular:

- $\mathbf{r}(t) = [r_x(t), r_y(t), r_z(t)]^T$  is the instantaneous, absolute S/C position vector expressed in an Earth-Centered Inertial (ECI) reference frame (or, its realization in the J2000 frame);
- $\dot{\mathbf{r}}(t) = [\dot{r}_x(t), \dot{r}_y(t), \dot{r}_z(t)]^T$  is the instantaneous, absolute S/C velocity vector expressed in ECI frame;
- $\ddot{\mathbf{r}}(t) = [\ddot{r}_x(t), \ddot{r}_y(t), \ddot{r}_z(t)]^T$  is the instantaneous, absolute S/C acceleration vector expressed in ECI frame;
- $r(t)$  is the instantaneous geocentric distance of the S/C from the Earth center of mass (i.e.,  $r(t) = \|\mathbf{r}(t)\|$ )
- $\mu_e$  is the Earth's gravitational parameter ( $\mu_e = 398600.4405 \text{ km}^3 \text{ s}^{-2}$  based on (Montenbruck et al., 2002))

Time is the independent variable in the equations of motion for orbital navigation using GNSS measurements, which are tagged to the GPS Time (GPST). Transformations using International Atomic Time (TAI) are needed for transitions between dynamical and atomic time scales (Montenbruck et al., 2002). However, time dependence will be implicit hereafter and time variable will be omitted.

It is remarked that (4) undertakes the assumption of the Earth being a sphere that is gravitationally equivalent to point mass. Although a realistic Earth's gravitation model should account for the geopotential gradient due to the non-uniform mass distribution of the geoid, this first-order approximation is increasingly acceptable for orbital altitudes above 50 000 km (Montenbruck et al., 2002). As the S/C moves away from the Earth in the interplanetary trajectory towards the Moon, other perturbing forces become dominant, such as luni-solar gravitational fields and solar radiation pressure (SRP). Incorporating third-body effects into the S/C's orbital dynamics extends the two-body model into a multi-body problem. Since the physical realization of forces is additive in nature, the non-linear differential equation of perturbed orbital motion can be expressed following Cowell's formulation:

$$\ddot{\mathbf{r}} = -\frac{\mu_e \mathbf{r}}{r^3} + \ddot{\mathbf{r}}_p \quad (5)$$

The net perturbative acceleration  $\ddot{\mathbf{r}}_p$  to the spherically symmetric Earth's gravitation reads as:

$$\ddot{\mathbf{r}}_p = \ddot{\mathbf{r}}_{3b} + \ddot{\mathbf{r}}_{srp} \quad (6)$$

and it includes  $\ddot{\mathbf{r}}_{3b}$  the acceleration due to the point mass gravitation of other celestial bodies, and  $\ddot{\mathbf{r}}_{srp}$  the acceleration arising from solar photons impinging on the S/C surface.

Assuming a set of  $n_c$  celestial bodies, the first term of (6), resolved about ECI frame axes, is:

$$\ddot{\mathbf{r}}_{3b} = \sum_{j=1}^{n_c} \mu_j \left( \frac{\mathbf{r}_j - \mathbf{r}}{\|\mathbf{r}_j - \mathbf{r}\|^3} - \frac{\mathbf{r}_j}{r_j^3} \right) \quad (7)$$

where  $\mathbf{r}_j$  denotes the geocentric position vector of the  $j$ -th celestial body,  $r_j$  its distance from the Earth's center of mass, and  $\mu_j$  its planetary mass parameter. For GNSS-based navigation in deep-space up to cislunar altitudes and lunar orbits, (7) encompasses perturbations from the Sun and Moon. The geocentric positions of these celestial bodies can be retrieved from Jet Propulsion Laboratory (JPL) Development Ephemerides series DE440 (Park et al., 2021). These ephemerides, reference to the International Celestial Reference System (ICRS) (e.g., ECI-frame), and are computed by fitting integrated orbits to both ground-based and space-based observations in a series of Chebyshev polynomials. The DE series are time-tagged to Barycentric Coordinate Time (TCB), requiring conversions to align with GPST. The planetary mass parameters according to DE440 are tabulated in (Park et al., 2021).

The SRP induced acceleration on a S/C of mass  $m$  can be considered as a surface force which is approximated by the following spherical model (McMahon, 2011):

$$\ddot{\mathbf{r}}_{srp} = -P_{srp}^{1\text{AU}} \left( \frac{1\text{AU}}{\|\mathbf{r}_s - \mathbf{r}\|} \right)^2 \frac{A}{m} C_R \frac{\mathbf{r}_s - \mathbf{r}}{\|\mathbf{r}_s - \mathbf{r}\|} \quad (8)$$

156 where  $A$  is the S/C exposed area to solar energy,  $C_R$  is the radiation pressure coefficient (cf. Table 3.5 of (Montenbruck et al.,  
 157 2002)) that depends on the S/C reflectivity  $\epsilon$ , and  $\mathbf{r}_s$  is the ECI-frame position vector of the Sun. Assuming that  $A$  absorbs all  
 158 photons (i.e.,  $\epsilon = 0$ ) and is normal to the direction of the incoming radiation,  $P_{srp}^{1\text{AU}} \approx 4.56 \times 10^{-6} \text{ N m}^{-2}$  is the force of solar  
 159 pressure per unit area in one astronomical distance ( $1\text{AU} \approx 149.6 \times 10^6 \text{ km}$ ).

160 Building upon (1), the orbital dynamic model in an ECI-frame can be obtained as a variation of Cowell's formulation (6) into a  
 161 non-linear, first-order vector differential equation:

$$\frac{d}{dt} \underbrace{\begin{bmatrix} \mathbf{r} \\ \dot{\mathbf{r}} \end{bmatrix}}_{\mathbf{x}^{sc}} = \underbrace{\begin{bmatrix} \dot{\mathbf{r}} \\ -\frac{\mu_e \mathbf{r}}{r^3} + \ddot{\mathbf{r}}_{3b} + \ddot{\mathbf{r}}_{srp} \end{bmatrix}}_{\mathbf{f}(\mathbf{x}^{sc}, t)} + \begin{bmatrix} \mathbf{0}_{3 \times 1} \\ \mathbf{w}^{sc} \end{bmatrix} \quad (9)$$

162 where  $\mathbf{w}^{sc}$  is the instantaneous acceleration driving noise with Power Spectral Density (PSD)  $\mathbf{S}_w^{sc} = [S_{w_x}^{sc}, S_{w_y}^{sc}, S_{w_z}^{sc}]^T$ .

163 The differential model (9) is applicable for a deep-space orbital propagator during a transfer orbit above 50 000 km altitude, and  
 164 it is also suitable for cislunar and lunar altitudes. Recent contributions have considered a model in a selenocentric inertial frame  
 165 that incorporates higher-order lunar gravity harmonics (Iiyama et al., 2024). Nonetheless, this model lies beyond the scope of  
 166 the present study.

## 167 2. GNSS measurement model and clock dynamics

168 Sampled GNSS observations admit a non-linear functional model with the S/C positioning states. Assuming Time-Of-Arrival  
 169 (TOA) ranging based on code tracking, the pseudorange equation for the PRN sequence transmitted by the  $i$ -th GNSS satellite  
 170 is formulated at time  $t_k$  as:

$$\rho_k^i = \|\mathbf{r}_k - \mathbf{r}_k^i\| + c \cdot \delta t_{u,k} + \epsilon_k^i \quad (10)$$

171 where:

- 172 •  $\mathbf{r}_k^i$  is the position vector of the satellite center of mass at  $t_k$ ;
- 173 •  $\delta t_{u,k}$  is the receiver clock offset relative to GNSS system time at  $t_k$ ;
- 174 •  $\epsilon_k^i$  is the non-systematic, residual model error which combines both signal-in-space user range error (SISRE) and user  
 175 equipment error (UEE) into the user equivalent range error (UERE) (Teunissen and Montenbruck, 2017).

176 The pseudorange equation (10) is valid under the assumption that space-segment corrections, relativistic effects, atmospheric  
 177 delays<sup>2</sup>, and biases have been compensated for by external data or physical models (Teunissen and Montenbruck, 2017). The  
 178 position vector  $\mathbf{r}_k$  is referenced to the phase center of the GNSS receiver antenna onboard the S/C, unlike Section II.1, which  
 179 considers the position relative to the S/C center of gravity. A lever-arm correction factor should be applied to account for such  
 180 spatial offset. For a GNSS receiver tracking PRN sequences of both GPS and Galileo satellites,  $\delta t_{u,k}$  represents the clock-offset  
 181 relative to GPST. As such, the Galileo pseudorange equation must include an additional term for the GPS-to-Galileo time-offset  
 182 (GGTO). This GGTO can either be obtained from the navigation message and applied as a space-segment correction or, if not  
 183 demodulated, included as an unknown parameter in the sequential estimation process. The former approach is considered in the  
 184 observation model formulation according to Section II.3. Moreover, the satellite position vector in (10), whether computed from  
 185 broadcast ephemeris parameters in the navigation message or through precise orbit products, is determined in an Earth-Centered  
 186 Earth-Fixed (ECEF) frame (i.e., WGS84) (Teunissen and Montenbruck, 2017). Since the receiver position vector is more  
 187 conveniently expressed in an ECI frame, a rotational transformation is required to compare on-board GNSS measurements with  
 188 satellite positions.

189 Doppler measurements arise from the relative motion between the receiver and GNSS satellites, and they are relevant to the  
 190 estimation of both the receiver velocity and the frequency deviation of the receiver clock. The Doppler model can be derived by  
 191 differentiating the pseudorange equation with respect to time, and is computed from the projection of the relative satellite-receiver  
 192 velocity vector onto the receiver-to-satellite Line-of-Sight (LOS) (Morichi et al., 2024). For the tracked carrier component of  
 193 the  $i$ -th GNSS satellite, the Doppler measurement  $D_k^i$  is expressed as:

$$\underbrace{\dot{\rho}_k^i - \dot{\mathbf{r}}_k^i \cdot \mathbf{e}_k^i}_{D_k^i} = -\mathbf{e}_k^i \cdot \dot{\mathbf{r}}_k + c \cdot \delta \dot{t}_{u,k} + \dot{\epsilon}_k^i \quad (11)$$

<sup>2</sup>When tracking signals on multiple frequency bands, the dispersive group delay induced by the ionosphere is referenced to a single frequency using frequency-dependent ionospheric coefficients.

194 where:

- 195 •  $\dot{\rho}_k^i$  is the pseudorange-rate measurement at  $t_k$ ;
- 196 •  $\dot{\mathbf{r}}_k^i$  is the velocity vector of the satellite center of mass at  $t_k$ ;
- 197 •  $\mathbf{e}_k^i = [e_{x,k}^i, e_{y,k}^i, e_{z,k}^i]^T$  is the unit pointing vector from the S/C position to  $i$ -th satellite position at  $t_k$ ;
- 198 •  $\delta\dot{t}_{u,k}$  is the receiver oscillator frequency deviation (i.e., clock drift);
- 199 •  $\dot{\epsilon}_k^i$  is the residual error after model-based corrections and compensation of known physical effects.

200 Eventually, clock dynamics can be modelled using to the following discrete-time, linear stochastic system (Galleani, 2008):

$$\underbrace{\begin{bmatrix} \delta t_{u,k} \\ \delta \dot{t}_{u,k} \end{bmatrix}}_{\mathbf{x}_k^{clk}} = \underbrace{\begin{bmatrix} 1 & \Delta t \\ 0 & 1 \end{bmatrix}}_{\Phi^{clk}} \underbrace{\begin{bmatrix} \delta t_{u,k-1} \\ \delta \dot{t}_{u,k-1} \end{bmatrix}}_{\mathbf{x}_{k-1}^{clk}} + \underbrace{\begin{bmatrix} w_{\phi,k}^{clk} \\ w_{f,k}^{clk} \end{bmatrix}}_{\mathbf{w}_k^{clk}} \quad (12)$$

201 where  $\Delta t = t_k - t_{k-1}$ ,  $\Phi^{clk}$  is the time-invariant state-transition matrix, and  $\mathbf{w}_k^{clk}$  is the white noise random sequence (i.e.,  
202 from discretization of clock noise random walk) with stationary covariance  $\mathbf{Q}^{clk}$  (cf. Section 9.3 in (Brown and Hwang, 1992)).

### 203 3. State-space model formulation

204 Combining S/C orbital dynamics with the GNSS receiver clock states, the state vector for GNSS-based orbital navigation can  
205 be defined at time  $t_k$ :

$$\mathbf{x}_k = \begin{bmatrix} \mathbf{x}_k^{scT} & \mathbf{x}_k^{clkT} \end{bmatrix}^T \in \mathbb{R}^{n \times 1} \quad (13)$$

206 where  $\mathbf{x}_k^{sc} \in \mathbb{R}^{6 \times 1}$  includes the S/C absolute position and velocity vector states at time  $t_k$ , and  $n = 8$  for the present study.  
207 Starting from the non-linear, differential model (9) for perturbed orbital motion, an approximate linear model between sample  
208 times can be derived by linearizing around the latest estimate of S/C dynamics (i.e.,  $\hat{\mathbf{x}}_{k-1}^{sc}$ ). The solution to the first-order, vector  
209 differential equation of the state-transition matrix can be expressed as a function of the system matrix (Bar-Shalom et al., 2004):

$$\Phi_{k-1,k}^{sc} = e^{\mathbf{F}^{sc}(t, \hat{\mathbf{x}}_{k-1}^{sc}) \Delta t} \quad (14)$$

210 where:

$$\mathbf{F}^{sc}(t, \hat{\mathbf{x}}_{k-1}^{sc}) = \left. \frac{\partial \mathbf{f}(\mathbf{x}^{sc}, t)}{\partial \mathbf{x}^{sc}} \right|_{\mathbf{x}^{sc} = \hat{\mathbf{x}}_{k-1}^{sc}} = \begin{bmatrix} \mathbf{0}_{3 \times 3} & \mathbf{I}_{3 \times 3} \\ \frac{\partial}{\partial \mathbf{r}} \left( -\frac{\mu_e \mathbf{r}}{r^3} + \ddot{\mathbf{r}}_{3b} + \ddot{\mathbf{r}}_{srp} \right) \Big|_{\mathbf{x}^{sc} = \hat{\mathbf{x}}_{k-1}^{sc}} & \mathbf{0}_{3 \times 3} \end{bmatrix}. \quad (15)$$

211 The partial derivatives of Earth's point mass gravitation, third-body effects, and SRP can be found in (Montenbruck et al., 2002).  
212 From (14), the state-transition matrix for the linearized dynamics is obtained via Taylor series approximation. The linearized  
213 approximation may be inaccurate compared to the true transition matrix. An alternative is to express the differential equation  
214 of the state-transition matrix in variational form, and use numerical integration (Montenbruck et al., 2002). A simpler approach  
215 is to use a complex-step derivative approximation (Capuano, 2016).

216 Assuming a first-order Taylor approximation of (14), the state-transition matrix including receiver clock states takes the form:

$$\Phi_{k-1,k} = \begin{bmatrix} \mathbf{I}_{6 \times 6} + \mathbf{F}^{sc}(t, \hat{\mathbf{x}}_{k-1}^{sc}) \Delta t & \mathbf{0}_{6 \times 2} \\ \mathbf{0}_{2 \times 6} & \Phi^{clk} \end{bmatrix}. \quad (16)$$

217 Discretizing the process driving noise in (9) into a white noise sequence  $\mathbf{w}_k^{sc}$ , the covariance matrix of the discrete process  
218 sequence affecting state-transition dynamics becomes:

$$\mathbf{Q}_k = \begin{bmatrix} \mathbf{Q}_k^{sc} & \mathbf{0}_{6 \times 2} \\ \mathbf{0}_{2 \times 6} & \mathbf{Q}^{clk} \end{bmatrix}, \quad \mathbf{Q}_k^{sc} = \begin{bmatrix} \frac{\Delta t^3}{3} & \frac{\Delta t^2}{2} \\ \frac{\Delta t^2}{2} & \Delta t \end{bmatrix} \otimes \text{diag}(\mathbf{S}_{\mathbf{w}_k}^{sc}) \quad (17)$$

219 where  $\mathbf{S}_{\mathbf{w}_k}^{sc} = [S_{w_x,k}^{sc}, S_{w_y,k}^{sc}, S_{w_z,k}^{sc}]^T$  is the sampled PSD of the acceleration process white noise.

220 In a similar vein, the non-linear GNSS observation model (cf. Section II.2) can be linearized by taking the partials of the  
 221 measurements about the state evaluated locally at the sample instant. Assuming  $N_s$  tracked GPS/Galileo satellites at time  $t_k$   
 222 and GGTO demodulation (i.e., single constellation model), the Jacobian of the observation equations (10) and (11) is computed  
 223 as:

$$\mathbf{H}_k = \begin{bmatrix} \tilde{\mathbf{H}}_k & \mathbf{0}_{N_s \times 3} & c \cdot \mathbf{1}_{N_s \times 1} & \mathbf{0}_{N_s \times 1} \\ \mathbf{0}_{N_s \times 3} & \tilde{\mathbf{H}}_k & \mathbf{0}_{N_s \times 1} & c \cdot \mathbf{1}_{N_s \times 1} \end{bmatrix}, \quad \tilde{\mathbf{H}}_k = \begin{bmatrix} -e_k^1, \dots, -e_k^{N_s} \end{bmatrix}^T. \quad (18)$$

224 This linearized measurement model is valid under the assumption of processing single-frequency, code-based observations. For  
 225 dual-frequency processing, (18) strictly holds after ionosphere-free linear combination (Teunissen and Montenbruck, 2017).

226 When considering the processing of GNSS observations in a Kalman-based estimator, measurement noise  $\mathbf{v}_k$  is modeled as  
 227 a white random sequence with non-stationary covariance  $\mathbf{R}_k$ . The latter assumption is reasonable given the highly-variable  
 228 GNSS signal characteristics as a function of the S/C altitude, and thus over time. For  $N_s$  pseudorange and pseudorange-rate  
 229 observations available from navigation satellites, the covariance matrix is compactly written as:

$$\mathbf{R}_k = \text{diag} \left( \left[ \sigma_{\epsilon_k^{1,S}}^2, \dots, \sigma_{\epsilon_k^{N_s,S}}^2, \sigma_{\dot{\epsilon}_k^{1,S}}^2, \dots, \sigma_{\dot{\epsilon}_k^{N_s,S}}^2 \right] \right). \quad (19)$$

230 For the stochastic disturbance affecting pseudorange observations, the error budget in terms of UERE includes space-segment  
 231 errors (i.e., satellite clock and ephemeris parameters), uncorrected atmospheric effects, relativistic errors, and receiver noise.

232 The dominant contributor to receiver noise on pseudorange measurements is the code tracking jitter from the Delay-Lock Loop  
 233 (DLL), induced by thermal noise. The model from (Betz and Kolodziejcki, 2000), valid for BPSK modulated codes<sup>3</sup>, can be  
 234 used to weight code tracking accuracy runtime by jointly accounting for code loop tuning, front-end bandwidth, and received  
 235 Carrier-to-Noise-density ratio ( $C/N_0$ ).

236 Doppler measurements variance, instead, should account for the Phase-Lock Loop (PLL) carrier tracking jitter, influenced by  
 237 thermal noise and short-term Allan deviation, and Frequency-Lock Loop (FLL) frequency tracking jitter, primarily affected by  
 238 thermal noise, neglecting vibration-induced errors.

239 For a comprehensive understanding of each noise source, the reader is encouraged to refer to the literature on the topic (Kaplan  
 240 and Hegarty, 2017).

### III. METHODOLOGY

#### 1. UKF architecture with orbital propagator

242 For non-linear transitional models, the sub-optimal EKF uses a Taylor series approximation under the Gaussian assumption for  
 243 covariance prediction, while state-propagation can be achieved through numerical integration. In contrast, the UKF uses the  
 244 Unscented Transform (UT) paradigm, which can directly capture the moments of a target Gaussian distribution, providing a  
 245 more accurate representation of highly non-linear functions in sequential estimation. This section discusses the UKF model  
 246 embedded with an orbital propagator for GNSS-based sequential OD. The EKF-based model is not extensively discussed, as it  
 247 is well-documented in the literature (Capuano, 2016). However, the results section will evaluate both Bayesian models in the  
 248 task of S/C orbital navigation in LLO, when GNSS observations are filtered in a tightly integrated configuration.

249 Following the augmented form of the UKF (Särkkä and Svensson, 2023) with process noise terms, the augmented posterior  
 250 state estimate at  $t_{k-1}$  is expressed<sup>4</sup> as:

$$\hat{\mathbf{x}}_{k-1}^a = \begin{bmatrix} \hat{\mathbf{x}}_{k-1}^T & \mathbf{0}_{1 \times n} \end{bmatrix}^T. \quad (20)$$

251 Correspondingly, the augmented posterior covariance estimate follows as:

$$\hat{\mathbf{P}}_{k-1}^a = \begin{bmatrix} \hat{\mathbf{P}}_{k-1} & \mathbf{0}_{n \times n} \\ \mathbf{0}_{n \times n} & \mathbf{Q}_k \end{bmatrix}. \quad (21)$$

252 A set of  $2n + 1$  sigma-points are then deterministically computed as:

$$\boldsymbol{\chi}_{k-1}^i = \begin{bmatrix} \left( \boldsymbol{\chi}_{k-1}^{i,\mathbf{x}} \right)^T & \left( \boldsymbol{\chi}_{k-1}^{i,\mathbf{w}} \right)^T \end{bmatrix}^T = \begin{cases} \boldsymbol{\chi}_{k-1}^0 = \hat{\mathbf{x}}_{k-1}^a & \text{for } i = 0 \\ \boldsymbol{\chi}_{k-1}^i = \hat{\mathbf{x}}_{k-1}^a + \sqrt{(n + \lambda) \left[ \hat{\mathbf{P}}_{k-1}^a \right]_i} & \text{for } i = 1, \dots, n \\ \boldsymbol{\chi}_{k-1}^{i+n} = \hat{\mathbf{x}}_{k-1}^a - \sqrt{(n + \lambda) \left[ \hat{\mathbf{P}}_{k-1}^a \right]_i} & \text{for } i = n + 1, \dots, 2n \end{cases} \quad (22)$$

<sup>3</sup>When processing subcarrier modulated codes, the modified formulation discussed in (Betz, 2000) should be used. Yet for the processing of Galileo E5 and E5ab signals, code tracking error models can be found in (Tawk et al., 2012).

<sup>4</sup>For discrete-time equivalent models, the additive discrete process sequence has the same dimensionality of the state vector. However, this is not true in general, and a similar equivalence does not hold for model noises defined directly in discrete time (Gustafsson and Gustafsson, 2000)



253 where  $[\cdot]_i$  denotes the  $i$ -th matrix column, and the square-root of a matrix is computed from the Cholesky decomposition of the  
 254 positive definite  $\hat{P}_{k-1}^a$ . The terms of  $\chi_{k-1}^i$  can be further decomposed as:

$$\chi_{k-1}^{i,\mathbf{x}} = \left[ \left( \chi_{k-1}^{i,sc} \right)^T \left( \chi_{k-1}^{i,clk} \right)^T \right]^T ; \chi_{k-1}^{i,\mathbf{w}} = \left[ \mathbf{0}_{1 \times 3} \left( \chi_{k-1}^{i,w^{sc}} \right)^T \left( \chi_{k-1}^{i,w^{clk}} \right)^T \right]^T \quad (23)$$

255 to differentiate between the components relative to S/C positioning states and those relative to the GNSS receiver clock.  
 256 Equation (22) defines the scaled UT (Van Der Merwe, 2004) with

$$\lambda = \alpha^2 (n + \kappa) - n \quad (24)$$

257 determining the spread of the sigma-points around the mean of the posterior state density; this spread is tuned through the filter  
 258 parameters  $(\alpha, \kappa)$ . The sigma-points are assigned a set of scalar, time-invariant weights:

$$W_i = \begin{cases} \frac{\lambda}{n+\lambda} & i = 0 \\ \frac{1}{2(n+\lambda)} & i = 1, \dots, 2n \end{cases} \quad (25)$$

259 a) *Moments of the Gaussian prior state density*

$$\hat{\mathbf{x}}_k^- = \sum_{i=0}^{2n} W_i \chi_{k|k-1}^{i,\mathbf{x}} \quad (26)$$

$$\hat{P}_k^- = \sum_{i=0}^{2n} W_i \left[ \chi_{k|k-1}^{i,\mathbf{x}} - \hat{\mathbf{x}}_k^- \right] \left[ \chi_{k|k-1}^{i,\mathbf{x}} - \hat{\mathbf{x}}_k^- \right]^T .$$

260 The term  $\chi_{k|k-1}^{i,\mathbf{x}}$  is obtained through numerical integration of  $(\chi_{k-1}^{i,sc}, \chi_{k-1}^{i,w^{sc}})$  based on (9), and linear propagation of  
 261  $(\chi_{k-1}^{i,clk}, \chi_{k-1}^{i,w^{clk}})$  via (12). The predicted covariance evaluates the spread of the time propagated sigma-points over the  
 262 estimated mean of the prior. For the  $i$ -th time-propagated sigma-point  $\chi_{k|k-1}^{i,\mathbf{x}}$ , the predicted GNSS measurement vector  $\hat{z}_k^i$  is  
 263 calculated by leveraging the non-linear functional models (10) and (11). The predicted GNSS measurement vector would then  
 264 be computed:

$$\hat{z}_k = \sum_{i=0}^{2n} W_i \hat{z}_k^i \quad (27)$$

265 b) *Posterior estimation*

$$\mathbf{P}_{\mathbf{xz}} = \sum_{i=0}^{2n} W_i \left[ \chi_{k|k-1}^{i,\mathbf{x}} - \hat{\mathbf{x}}_k^- \right] \left[ \hat{z}_k^i - \hat{z}_k \right]^T$$

$$\mathbf{P}_{\mathbf{zz}} = \sum_{i=0}^{2n} W_i \left[ \hat{z}_k^i - \hat{z}_k \right] \left[ \hat{z}_k^i - \hat{z}_k \right]^T \quad (28)$$

$$\hat{\mathbf{x}}_k = \hat{\mathbf{x}}_k^- + \mathbf{P}_{\mathbf{xz}} \mathbf{P}_{\mathbf{zz}}^{-1} (\mathbf{z}_k - \hat{z}_k)$$

$$\hat{P}_k = \hat{P}_k^- - \mathbf{P}_{\mathbf{xz}} \mathbf{H}_k^T - \mathbf{H}_k \mathbf{P}_{\mathbf{xz}}^T + \mathbf{H}_k \mathbf{P}_{\mathbf{zz}} \mathbf{H}_k^T$$

266 where  $\mathbf{z}_k$  is the GNSS measurement vector at the sample instant (cf. Section II.2),  $\mathbf{P}_{\mathbf{xz}}$  is the the cross-covariance between  
 267  $\hat{\mathbf{x}}_k^-$  and  $\hat{z}_k$ , and  $\mathbf{P}_{\mathbf{zz}}$  is the innovation covariance (Julier et al., 2000). The last relation of (28) expresses a generalized Joseph  
 268 formula for the posterior covariance estimation, applicable to non-linear measurement models (Zanetti and DeMars, 2013).

## 269 2. Lunar orbit scenario

270 The upcoming LuGRE mission is considered as case-study to assess the potential of more complex non-linear Bayesian  
 271 formulations when tackling the challenges of autonomous orbital navigation of a S/C in the lunar regime.

272 The initial state-vector of the BGMI lander has been used in Ansys Systems Tool Kit (STK) to retrieve ephemeris parameters  
 273 for the whole mission based on the High Precision Orbit Propagator (HPOP). The ephemeris parameters are expressed in the

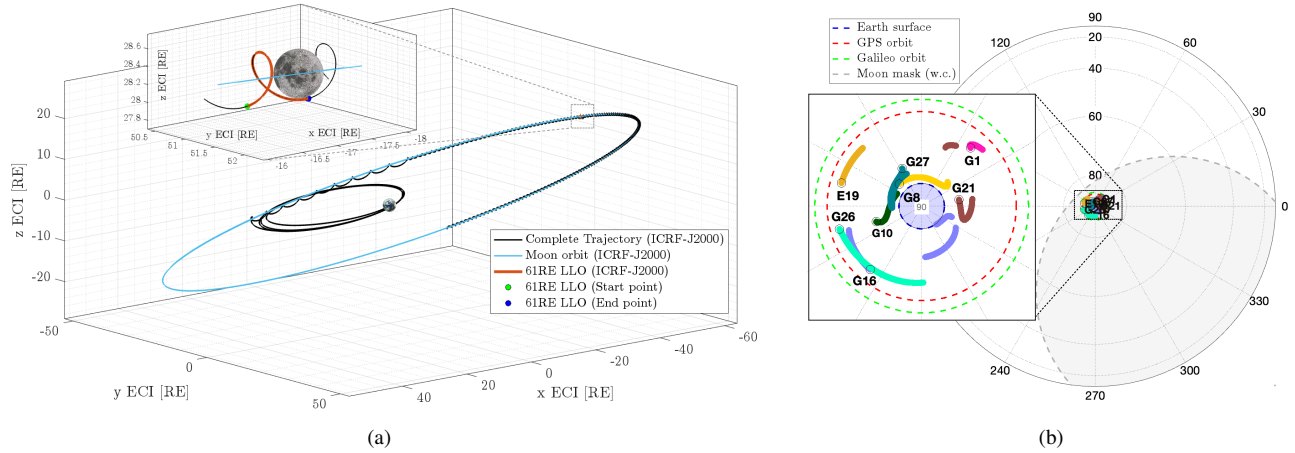


**Figure 2:** (a) The BGM1 lander trajectory with a zoom in the analyzed LLO segment. (b) The dynamic skyplot of tracked GPS and Galileo satellites in lunar proximity.

**Table 1:** Overview of the analyzed LuGRE mission segment in LLO.

Parameter	Value
Trajectory Type	LLO
Reference Frame	ICRF (ECI-J2000 realization)
Initial geocentric distance [km] (RE)	389032.47 (60.99)
Maximum geocentric distance [km] (RE)	390981.82 (61.30)
Mean geocentric distance [km] (RE)	389206.46 (61.02)
Initial GPS time [s] / UTCG date	1411329668.38 / 25-Sep-2024 20:01:49.382
Final GPS time [s] / UTCG date	1411336800.38 / 25-Sep-2024 21:59:42.382
Sampling time [s]	60

geocentric, inertial J2000 frame, and are converted to position and velocity states. Starting from the complete mission trajectory (45.97 days), a section (2 hours) has been selected for the evaluation of the navigation algorithms. This section has been chosen because it reflects the mission's scientific objectives and is characterized by particularly challenging navigation conditions, including limited availability of satellite measurements and degraded geometry. It involves a selenocentric segment in LLO around 61 Earth Radii (RE) and close to apolune, happening after the second Lunar Orbit Injection (LOI) maneuver (Parker et al., 2022). The LuGRE trajectory together with the analyzed LLO section are shown in Figure 2(a). Moreover, the LLO details are summarized in Table 1. For the selected LLO, the original 60-second step trajectory was up-sampled to 1 Hz performing 7-th order Lagrange interpolation in General Mission Analysis Tool (GMAT) (Hughes et al., 2014). This step was performed in view of emulating the operational scenario of the LuGRE receiver (cf. Section III.3). Eventually, a frame transformation to an Earth-fixed frame (ECEF-WGS84 realization) was operated on the up-sampled trajectory segment by accounting for Earth's rotational effects relative to inertial space.

The reported trajectory is based on pre-launch orbit design and does not reflect the actual trajectory the BGM1 lander will follow upon deployment. Details of the operational orbit remain undisclosed.

### 3. RF simulation framework & navigation analysis

To emulate the GNSS operational environment and the RF signal conditions the LuGRE receiver is expected to be subject to in the LLO segment, a multi-GNSS simulation model was configured in Spirent GSS9000 GNSS RF simulator (Spirent, 2015). Consistent with the NEIL hardware design and Earth GNSS signal processing capabilities, only GPS (G) and Galileo (E) constellations were modelled in the simulation environment. The most recent Almanac data and space-segment operational advisories were incorporated into the navigation systems' configuration. Although also other services are broadcast by the respective satellite payloads, the RF signal generation was confined to L1 C/A and L5 signals for GPS, and E1 and E5a signals for Galileo. For the Global Positioning System (GPS) constellation, the gain patterns of batches IIR and IIR-M were modelled according to (Marquis, 2016), with the boresight EIRP configured based on (Delépaut et al., 2020) for L1 C/A and L5-Q signals. Similarly, the gain pattern for batch IIF was taken from (Donaldson et al., 2020), and replicated for batch III-A. For the Galileo

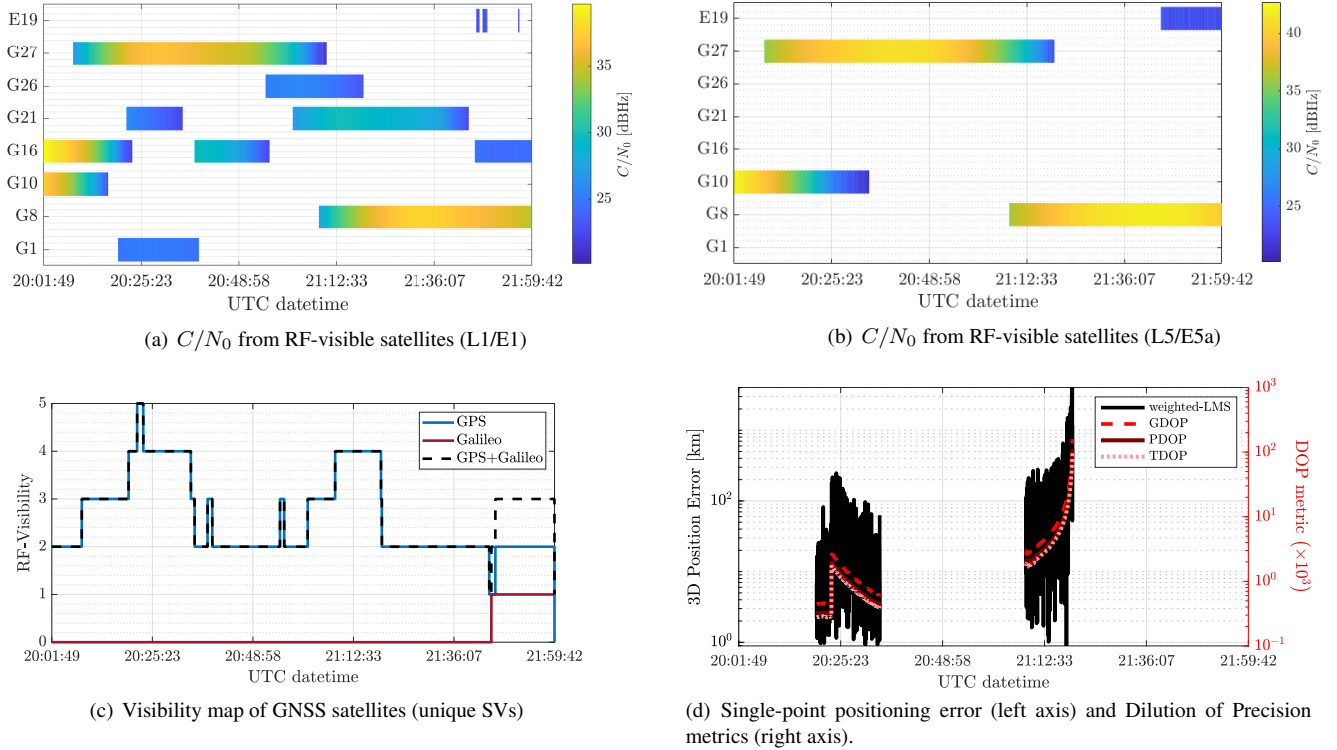


**Figure 3:** GNSS environment seen by the LuGRE receiver in the analyzed LLO segment in terms of relevant navigation metrics.

297 constellation, instead, patterns were configured based on the reference model for first generation Full Operational Capability  
 298 (FOC) satellite antennas (Menzione et al., 2024). Moreover, the non-isotropic radiation patterns of both GNSS systems for the  
 299 modelled signals were truncated with an off-boresight mask to account for satellite body effects. Further insights about RF link  
 300 simulation can be found in (Tedesco et al., 2023).

301 Regarding atmospheric effects, GNSS signals received from satellites on the opposite side of the Earth relative to the S/C's  
 302 position cross the ionosphere twice, causing greater delays and introducing unmodelled biases in the retrieved measurements.  
 303 These signals correspond to the main lobe portion in the transmitting EIRP that spills over the Earth's disk and is confined  
 304 within the altitude of the ionospheric layer (i.e.,  $\approx 10^3$  km). For GPS satellites, this translates to an angle of approximately  
 305  $13^\circ$  in the EIRP pattern, with an additional  $2.2^\circ$  margin for the ionosphere, while for Galileo satellites, the angles are slightly  
 306 smaller at approximately  $12^\circ$  plus  $2^\circ$  respectively, due to the higher orbit radius. At Moon altitudes, the likelihood of receiving  
 307 such signals is very low, as demonstrated in the feasibility study by (Delépaut et al., 2020). Therefore, ionospheric effects  
 308 were neglected in the simulation, which is justified for the analyzed LLO section of the LuGRE trajectory. Nevertheless, when  
 309 tracking dual-band signals for the same satellite and processing observables, ionospheric-free measurements can be obtained,  
 310 albeit with higher noise variance.

311 Based on the described framework, a HIL test was conducted by integrating the NEIL receiver in the configured GNSS testbench.  
 312 Digitally generated signals for GPS L1/L5 and Galileo E1/E5a bands were upconverted to RF and transmitted through Spirent's  
 313 Signal Generator Unit (SGU). RF signals were eventually processed by the LuGRE receiver, thus allowing the record and  
 314 post-processing of dual-band raw measurements from both constellations.

315 Figure 2(b) displays the dynamic skyplot of GPS and Galileo satellites, whose signals are tracked and for which observables are  
 316 constructed, according to the high-sensitivity acquisition and tracking capabilities of the LuGRE receiver. This polar diagram  
 317 considers the instantaneous relative dynamics between the S/C and the tracked GNSS satellites in the LLO segment. The  
 318 positions and velocities of the tracked GNSS satellites are projected onto a Local Vertical Local Horizontal (LVLH) frame (for  
 319 Space Data Systems, CCSDS), with the radial direction representing the S/C's boresight, assuming perfect pointing to the  
 320 Earth's center of mass. To ease graphical interpretation, a zoom is included that frames the boresight direction; it is clearly  
 321 visible that the batch of tracked satellites is clustered at boresight thus lacking variability in elevation due to the large distance  
 322 of the S/C from the Earth compared to the GPS/Galileo orbit semi-major axis. Moreover, the minimum elevation for the Earth's  
 323 disk and the elevation isolines of both GPS and Galileo systems are identified by modeling the GNSS system's orbit semi-major

324 axis and flattening. For each S/C position, an ellipsoid is considered, and the minimum elevation level is determined and  
 325 repeated over the entire analyzed LLO. This elevation isoline represents the boundary circle beyond which satellites cannot be  
 326 seen inside the polar diagram. The Moon’s occlusion of the S/C-to-Earth LOS is considered as well instant-by-instant, with the  
 327 skyplot representing the worst-case Moon occupation. Despite this occlusion, RF signals are not necessarily blocked. Given  
 328 the S/C’s mean geocentric distance (cf. Table 1) and the Moon’s radius (about 0.2727 of Earth’s mean equatorial radius), the  
 329 Moon’s disk occupies an angle roughly 84.19 times smaller than the Galileo E1 main lobe beamwidth when the Moon center of  
 330 mass is taken collinear with the S/C-to-Earth LOS.

331 By setting a 20 dB-Hz threshold as the minimum received  $C/N_0$  level of a signal for the corresponding raw observable to be  
 332 considered available for processing in the PVT unit, the  $C/N_0$  patterns seen by the LuGRE receiver are depicted in Figure 3(a)  
 333 for L1/E1 band and in Figure 3(b) for the L5/E5a band. For the mean geocentric distance of the analyzed LLO, a 30 dB-Hz  
 334 threshold is reasonable to differentiate between the reception of the main lobe and peak side lobes. The measured  $C/N_0$  levels  
 335 for L5/E5a band signals are higher, reaching up to 43 dB-Hz for GPS L5, due to the wider transmission pattern beamwidth and  
 336 lower path loss. This aligns with the observations by (Delépaut et al., 2020). However, more signals are tracked on the L1/E1  
 337 band because only a subset of satellites of each system broadcasts services in the lower frequency band. Notably, measurements  
 338 are available from only one Galileo satellite (i.e., E19) in the whole LLO segment, with a side lobe signal being tracked. This  
 339 is likely caused by the conservative modeling of Galileo EIRP in the simulator, or the orbital geometry, as Galileo satellites are  
 340 distributed across three orbital planes compared to GPS’s six, limiting orbital diversity.

341 Figure 3(c) illustrates the radiometric visibility profile of GNSS satellites throughout the entire LLO section. It shows that a  
 342 maximum of five GPS satellites are tracked for a short interval of 130 s, accounting for only the 1.21% of the dataset length. On  
 343 average, 2.72 satellites are tracked, indicating that fewer than three satellites are available for most of the dataset. Moreover,  
 344 the availability of the minimum number of measurements required for the computation of a single-point PVT solution is 21.32%.  
 345 This availability is reflected in the weighted Least-Mean Squares (LMS) solution shown in Figure 3(d) (left axis). The right axis  
 346 on the same figure highlights the profiles of geometric DOP (GDOP), position DOP (PDOP), and time DOP (TDOP). To better  
 347 illustrate the dependence of the single-point positioning error on the DOP metrics, a logarithmic scale was chosen. Due to the  
 348 scarcity of tracked GNSS satellites, the LLO scenario is characterized by remarkable DOP discontinuities. In particular, the  
 349 rapidly changing geometric conditions can be characterized by steep ascending ramps, which rapidly deteriorate the accuracy  
 350 of GNSS single-point estimates.

#### IV. RESULTS

351 This section discusses the OD performance of the UKF-based OF model (cf. Section III.1) within the analyzed LLO scenario  
 352 in the LuGRE framework, benchmarked against the renowned EKF-based model. The filtering-based algorithms are analyzed  
 353 for post-processing sampled GNSS observations collected by the LuGRE receiver in the HIL simulation (cf. Section III.3).  
 354 The filters have been developed with equivalent orbital propagators modeling S/C dynamics, and share the same stochastic  
 355 characterization of the noises affecting both the process and the measurements (cf. Section II.3). It is remarked that sequential  
 356 estimators require an initial condition for the PVT states, which models the prior knowledge about the system. Typically, this  
 357 initialization can be provided through a (weighted) single-point solution. However, the limited multi-system, multi-channel  
 358 position fixing availability observed in lunar proximity (cf. Figure 3) suggests the need for alternative approaches. For the  
 359 current assessment, aided initialization is assumed; in the real operational scenario, this approach would leverage data via the  
 360 ground-based TeleCommand (TC) link. Similarly, in this analysis, the navigation algorithms are initialized using the upsampled  
 361 BGM1 lander trajectory. To simulate inaccuracies in the aiding information, purposely degraded initialization is considered.  
 362 For the position states, a  $10^3$  m error is uniformly added to each spatial dimension. A similar approach is applied to the velocity  
 363 states, with a smaller error accounting for the 0.1 % of the true lander speed at the initial sample time. In the absence of reference  
 364 values for the receiver timing states, approximate values of  $10^3$  m and  $10^{-4}$  m s $^{-1}$  are assigned, and this lack of prior knowledge  
 365 is modelled in the covariance of the initial state distribution.

366 Figure 4 shows the time-series of S/C position and velocity estimation errors (ECI frame) using dual-channel GNSS observations,  
 367 with separate plots for position (Figure 4(a)) and velocity (Figure 4(b)). The solid lines of each error subplot evaluate the distance  
 368 of the estimated mean of the posterior density from the true lander positioning state at the sample instant. Moreover, the shaded  
 369 areas indicate the conditional 3-sigma Root-Sum-Squared (RSS) error. Figure 5 presents the errors in the S/C comoving orbital  
 370 frame, separating radial error from the orthogonal plane components. Cumulative error statistics are summarized in Table 2.

371 Upon the biased initialization of  $10^3$  m, the radial position error in Figure 5(a) reduces to about 50m after the first sample of  
 372 GNSS observations are filtered through to orbital propagator. Given that the tracked satellites are clustered at high elevation  
 373 (cf. 2(b)), the radial error mirrors the error in the receiver clock offset estimate. A similar behavior characterizes the radial  
 374 component of the velocity estimate, as shown in Figure 5(b). Despite the limited number of available measurements at the  
 375 beginning of the LLO section, the receiver timing states possess enough observability to allow for the convergence of the radial  
 376 estimate. Conversely, the normal component exhibits an error bigger than the initial mismatch and takes longer time (about 10

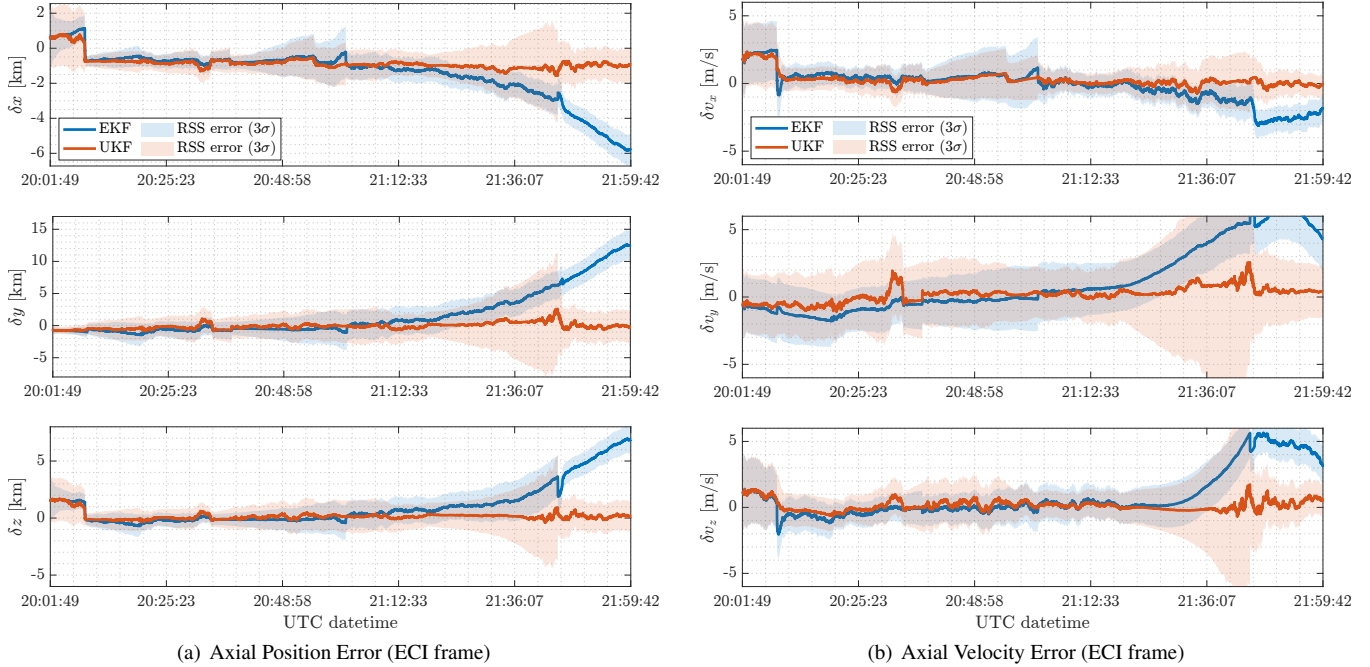


**Figure 4:** EKF and UKF OD error (solid line) with RSS confidence intervals (shaded area) at  $3\sigma$  (99.7% confidence).

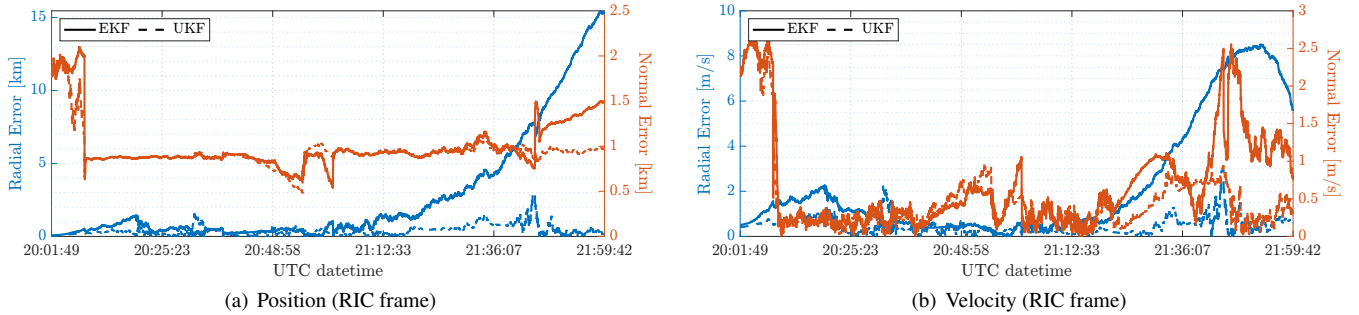


**Figure 5:** EKF and UKF OD error decomposed in radial (left axis) and normal (right axis) components of a local orbital frame.

377 minutes) to reduce for both filters. Additionally, for the normal components, the mean posterior estimates remain biased by  
 378 roughly the same amount as the simulated initialization error. This suggests that accurate initialization is crucial for achieving  
 379 accurate OD solutions in operational scenarios with significant depletion of Earth GNSS signal, such as those experienced at  
 380 the Moon.

381 During the first time frame of single-point PVT availability (cf. Figure 3(d) between 20:20 and 20:34), the radial position and  
 382 velocity error profiles of both estimators follow the GDOP pattern as expected. However, at the end of the time frame, the UKF  
 383 radial position estimate exhibits a sudden deviation while the EKF remains stable. This phenomenon might be associated with  
 384 a decrease in the observability of the clock states due to the loss of L1 signal track for satellites G1 and G21 (cf. Figure 3(a)),  
 385 along with the UKF filter gain weighting more the observations than the EKF. Moreover, examining the entire LLO section,  
 386 abrupt variations in the radial error time series often coincide with discontinuities in the radiometric tracking of satellites (cf.  
 387 Figure 3(c)). These discontinuities can determine anomalies in the clock states' estimates, directly affecting the radial terms.  
 388 However, the UKF appears to be less affected by these effects, resulting in a smoother estimate overall.

389 More interesting effects can be observed during the second time frame of single-point PVT availability (cf. Figure 3(d) between  
 390 21:8 and 21:19), which is marked by a harmful PDOP ramp with values reaching nearly  $160 \times 10^3$ . At the end of this ramp,  
 391 coinciding with the loss of signal track for G1 on L1 band and G7 on L5, the conditional posterior estimates from the two  
 392 filters highlight different behaviors. the EKF posterior mean for both position and velocity states drifts, accumulating an error  
 393 against the true lander state that increases exponentially over time. This is clearly evidenced by the axial errors in Figure 4.

**Table 2:** Cumulative OD error statistics for EKF and UKF architectures.

Bayesian Filter	Position Error [km]				Velocity Error [m/s]			
	68.3%	95.5%	99.7%	100%	68.3%	95.5%	99.7%	100%
EKF	2.26	13.06	15.43	15.52	2.42	8.44	8.63	8.67
UKF	1.02	1.76	3.09	3.16	0.81	2.29	3.14	3.20

394 Despite the growing error, the EKF maintains high confidence in its estimate, as the  $3\sigma$  RSS error profile closely follows the  
395 OD error curves. This likely results from the non-linearity of the system dynamics, which compromises the validity of the EKF  
396 Taylor approximation about the latest state estimate. For each component of  $x_k^{sc}$ , comparing the terms of (15) evaluated both  
397 about the latest state estimate and about the true lander state, the difference between these quantities exceeds the corresponding  
398 state estimate’s uncertainty, leading to an overoptimistic covariance and a growing state estimation error. Conversely, the UKF  
399 posterior estimate maintains its accuracy, albeit the above mentioned bias on the normal component. Simultaneously, the UKF  
400 confidence in the estimate decreases exponentially, as indicated by the RSS error profile. This suggests that the UT-based  
401 approximation of the state density better accounts for unknown changes in the system dynamics in the absence of GNSS  
402 observations. Moreover, sigma-points enable an improved approximation of state correlations in the Gaussian belief, which is  
403 crucial for maintaining estimate quality under compromised state observability. In the final part of the LLO, new measurements  
404 from a Galileo satellite allow for a reduction in the UKF state uncertainty estimate. For the EKF, instead, the estimate is sensitive  
405 to changes in the observables’ set, but this is insufficient to recover from divergence.

## V. CONCLUSION

406 This study has demonstrated the performance of autonomous GNSS-based OD in the lunar regime. In a sequential Bayesian  
407 architecture which integrates GNSS radiometric observations tightly with the prediction of space dynamics from an orbital  
408 propagator, the potential of an UKF-based model has been investigated for statistical OD. The more complex sigma-point filter  
409 has been compared against the renown EKF-based OF model, showcasing near-Moon PNT at about 61 RE. The upcoming LuGRE  
410 scientific mission has served as case-study, selecting a LLO segment from a pre-launch design of the BGM1 trajectory. Both  
411 Bayesian navigation algorithms have been assessed through the post-processing of raw multi-band GPS/Galileo observables;  
412 these measurements have been constructed by the NEIL receiver in a HIL test with realistic RF link simulation.

413 By leveraging the UT under the Gaussian assumption, the UKF can better approximate the moments of the posterior belief for the  
414 latent state. When the state observability is undermined due to the absence of fresh measurements, enhanced OD performance  
415 can be pursued through better modelling the correlations of states while propagating orbital dynamics. This seems promising in  
416 scenarios with severe satellite signal depletion, such as in lunar proximity. Moreover, the UKF’s sigma-point sampling proves  
417 effective in maintaining estimate accuracy and mitigating the effects of harmful discontinuities characterizing multi-lateration  
418 geometry in the lunar regime.

419 Highlights of the study include:

- 420 • The UKF maintains position estimation errors within 2 km for the 98.97% of time over the analyzed dataset, with a net  
421  $3\sigma$  accuracy gain over the EKF of 79.97% for the position estimate and of 63.62% for the velocity estimate.
- 422 • Under detrimental GDOP conditions, the UKF results in a smoother and more resilient state estimate compared to the  
423 EKF; the latter exhibits a divergent trend driven by an overoptimistic covariance estimate.
- 424 • Accurate initialization might be critical for both filters, particularly in the lunar environment, where availability of  
425 radiometric observations is limited and mismatching biases can be hardly cancelled.
- 426 • The strong yet peculiar TDOP caused by the lack of elevation diversity in satellite ranging sources necessitates sequential  
427 estimators that can reduce the sensitivity of radial estimates to discontinuities in the timing estimates.

428 Aligning with the goals of increased autonomy, the UKF-based OF model seems to offer a promising solution for GNSS-based  
429 onboard OD in the lunar regime. Further research will aim to further enhance PNT algorithms, and GNSS-based OD will be  
430 explored in different deep-space and cis-lunar operational scenarios.

## ACKNOWLEDGEMENTS

431 This study was funded within the contract n. 2021-26-HH.0 ASI/Politecnico di Torino "Attività di R&S inerente alla Navigazione  
432 GNSS nello Space volume Terra/Luna nell’ambito del Lunar GNSS Receiver Experiment". O. Vouch acknowledges funding  
433 from the Politecnico di Torino Interdepartmental Centre for Service Robotics (PIC4SeR). A. Minetto acknowledges funding  
434 from the research contract no. 32-G-13427-5 DM 1062/2021 funded within the Programma Operativo Nazionale (PON) Ricerca

435 ed Innovazione of the Italian Ministry of University and Research (MUR).

## REFERENCES

- 436 Bar-Shalom, Y., Li, X. R., and Kirubarajan, T. (2004). *Estimation with applications to tracking and navigation: theory*  
437 *algorithms and software*. John Wiley & Sons.
- 438 Battin, R. H. (1999). *An introduction to the mathematics and methods of astrodynamics*. Aiaa.
- 439 Betz, J. W. (2000). Design and performance of code tracking for the gps m code signal. In *Proceedings of the 13th International*  
440 *Technical Meeting of the Satellite Division of The Institute of Navigation (ION GPS 2000)*, pages 2140–2150.
- 441 Betz, J. W. and Kolodziejcki, K. R. (2000). Extended theory of early-late code tracking for a bandlimited gps receiver. *Navigation*,  
442 47(3):211–226.
- 443 Brown, R. G. and Hwang, P. Y. (1992). Introduction to random signals and applied kalman filtering(book). *New York, John*  
444 *Wiley & Sons, Inc., 1992. 512*.
- 445 Capuano, V. (2016). Gnss-based navigation for lunar missions. Technical report, EPFL.
- 446 Capuano, V., Shehaj, E., Botteron, C., Blunt, P., and Farine, P.-A. (2017). Keynote: An adaptive gnss-based reduced dynamic  
447 approach for real time autonomous navigation from the earth to the moon. In *Proceedings of the ION 2017 Pacific PNT*  
448 *Meeting*, pages 331–347.
- 449 Delépaut, A., Giordano, P., Ventura-Traveset, J., Blonski, D., Schönfeldt, M., Schoonejans, P., Aziz, S., and Walker, R. (2020).  
450 Use of gnss for lunar missions and plans for lunar in-orbit development. *Advances in Space Research*, 66(12):2739–2756.
- 451 Donaldson, J. E., Parker, J. J., Moreau, M. C., Highsmith, D. E., and Martzen, P. D. (2020). Characterization of on-orbit gps  
452 transmit antenna patterns for space users. *NAVIGATION, Journal of the Institute of Navigation*, 67(2):411–438.
- 453 Fang, H., Tian, N., Wang, Y., Zhou, M., and Haile, M. A. (2018). Nonlinear bayesian estimation: From kalman filtering to a  
454 broader horizon. *IEEE/CAA Journal of Automatica Sinica*, 5(2):401–417.
- 455 for Space Data Systems (CCSDS), C. C. (2019). *CCSDS Report Concerning Navigation Data—Definitions and Conventions*.  
456 Washington, DC, USA, issue 4 edition. Green Book, Informational Report.
- 457 Galleani, L. (2008). A tutorial on the two-state model of the atomic clock noise. *Metrologia*, 45(6):S175.
- 458 Gustafsson, F. and Gustafsson, F. (2000). *Adaptive filtering and change detection*, volume 1. Wiley New York.
- 459 Hughes, S. P., Qureshi, R. H., Cooley, S. D., and Parker, J. J. (2014). Verification and validation of the general mission analysis  
460 tool (gmat). In *AIAA/AAS astrodynamics specialist conference*, page 4151.
- 461 Iess, L., Di Benedetto, M., James, N., Mercolino, M., Simone, L., and Tortora, P. (2014). Astra: Interdisciplinary study on  
462 enhancement of the end-to-end accuracy for spacecraft tracking techniques. *Acta Astronautica*, 94(2):699–707.
- 463 Iiyama, K., Bhamidipati, S., and Gao, G. (2024). Precise positioning and timekeeping in a lunar orbit via terrestrial gps  
464 time-differenced carrier-phase measurements. *NAVIGATION: Journal of the Institute of Navigation*, 71(1).
- 465 Julier, S., Uhlmann, J., and Durrant-Whyte, H. F. (2000). A new method for the nonlinear transformation of means and  
466 covariances in filters and estimators. *IEEE Transactions on automatic control*, 45(3):477–482.
- 467 Kaplan, E. and Hegarty, C. (2017). *Understanding GPS/GNSS: Principles and Applications*. Artech House.
- 468 Marquis, W. (2016). The gps block iir antenna panel pattern and its use on-orbit. In *Proceedings of the 29th International*  
469 *Technical Meeting of the Satellite Division of The Institute of Navigation (ION GNSS+ 2016)*, pages 2896–2909.
- 470 McMahon, J. W. (2011). *An analytical theory for the perturbative effect of solar radiation pressure on natural and artificial*  
471 *satellites*. PhD thesis, University of Colorado at Boulder.
- 472 Menzione, F., Sgammini, M., Paonni, M., et al. (2024). Reconstruction of galileo constellation antenna pattern for space service  
473 volume applications. *Publications Office of the European Union: Luxembourg*.
- 474 Minetto, A., Dovis, F., Nardin, A., Vouch, O., Impresario, G., and Musmeci, M. (2022). Analysis of GNSS data at the Moon  
475 for the LuGRE project. In *2022 IEEE 9th International Workshop on Metrology for AeroSpace (MetroAeroSpace)*, pages  
476 134–139. ISSN: 2575-7490.
- 477 Montenbruck, O., Gill, E., and Lutze, F. (2002). Satellite orbits: models, methods, and applications. *Appl. Mech. Rev.*,  
478 55(2):B27–B28.

- 479 Morichi, L., Minetto, A., Nardin, A., Zocca, S., and Dovis, F. (2024). Pseudorange and doppler-based state estimation from meo  
480 to leo: A comprehensive analysis of maximum likelihood estimators. In *Proceedings of the 2024 International Technical  
481 Meeting of The Institute of Navigation*, pages 677–691.
- 482 Murata, M. (2023). Ensemble kalman filter for moon transfer orbit gps navigation. In *Proceedings of the 2023 International  
483 Technical Meeting of The Institute of Navigation*, pages 204–212.
- 484 Nardin, A., Minetto, A., Guzzi, S., Dovis, F., Konitzer, L., and Parker, J. J. K. (2023). Snapshot tracking of GNSS signals in  
485 space: A case study at lunar distances. In *Proceedings of the 36th International Technical Meeting of the Satellite Division  
486 of The Institute of Navigation (ION GNSS+ 2023)*, pages 3267–3281, Denver, Colorado.
- 487 Nardin, A., Minetto, A., Vouch, O., Maiani, M., and Dovis, F. (2022). Snapshot acquisition of GNSS signals in space: a case  
488 study at lunar distances. In *Proceedings of the 35th International Technical Meeting of the Satellite Division of The Institute  
489 of Navigation (ION GNSS+ 2022)*, pages 3603 – 3617, Denver, Colorado.
- 490 Park, R. S., Folkner, W. M., Williams, J. G., and Boggs, D. H. (2021). The jpl planetary and lunar ephemerides de440 and  
491 de441. *The Astronomical Journal*, 161(3):105.
- 492 Parker, J. J., Bauer, F. H., Ashman, B. W., Miller, J. J., Enderle, W., and Blonski, D. (2018). Development of an interoperable  
493 gnss space service volume. In *Proceedings of the 31st International Technical Meeting of the Satellite Division of The Institute  
494 of Navigation (ION GNSS+ 2018)*, pages 1246–1256.
- 495 Parker, J. J., Dovis, F., Anderson, B., Ansalone, L., Ashman, B., Bauer, F. H., D’Amore, G., Facchinetti, C., Fantinato, S.,  
496 Impresario, G., et al. (2022). The Lunar GNSS Receiver Experiment (LuGRE). In *Proceedings of the 2022 International  
497 Technical Meeting of The Institute of Navigation (ION ITM 2022)*, pages 420–437.
- 498 Särkkä, S. and Svensson, L. (2023). *Bayesian filtering and smoothing*, volume 17. Cambridge university press.
- 499 Schutz, B., Tapley, B., and Born, G. H. (2004). *Statistical orbit determination*. Elsevier.
- 500 Spirent (2015). GSS9000 GNSS Simulator.
- 501 Tawk, Y., Botteron, C., Jovanovic, A., and Farine, P.-A. (2012). Analysis of galileo e5 and e5ab code tracking. *GPS solutions*,  
502 16:243–258.
- 503 Tedesco, S., Bernardi, F., Guzzi, S., Boschiero, M., Pulliero, M., Marcantonio, D., Ghedin, M., Miotti, E., Fantinato, S.,  
504 Pozzobon, O., et al. (2023). Deep space gnss in moon transfer orbit: the lugre receiver. In *2023 IEEE International  
505 Conference on Wireless for Space and Extreme Environments (WiSEE)*, pages 1–6. IEEE.
- 506 Teunissen, P. J. G. and Montenbruck, O. (2017). *Springer handbook of global navigation satellite systems*, volume 10. Springer.
- 507 Turan, E., Speretta, S., and Gill, E. (2022). Autonomous navigation for deep space small satellites: Scientific and technological  
508 advances. *Acta Astronautica*, 193:56–74.
- 509 Van Der Merwe, R. (2004). *Sigma-point Kalman filters for probabilistic inference in dynamic state-space models*. Oregon  
510 Health & Science University.
- 511 Vouch, O., Nardin, A., Minetto, A., Zocca, S., Valvano, M., and Dovis, F. (2024). Aided kalman filter models for gnss-based  
512 space navigation. *IEEE Journal of Radio Frequency Identification*, 8:535–546.
- 513 Zanetti, R. and DeMars, K. J. (2013). Joseph formulation of unscented and quadrature filters with application to consider states.  
514 *Journal of Guidance, Control, and Dynamics*, 36(6):1860–1864.